Published by IOP Publishing for Sissa Medialab

Received: May 12, 2026
Accepted: June 23, 2026
Published: July 20, 2026

21st Trento Workshop on Advanced Silicon Radiation Detectors
Perugia, Italy
17–19 February 2026

Development of a double-sided LGAD prototype from single-sided sensors: design, characterization, and proof of principle

Jerzy Pietraszko,[a,*] Maurizio Boscardin,[b] Ashish Bisht,[b] Thomas Bergauer,[c] Alfons Dehé,[i] Henrik Flörsheimer,[d] Jochen Frühauf,[a] Tetyana Galatyuk,[a,d,e] Harald Handerkas,[c,f] Henning Heggen,[a] Albert Hirtl,[f] Mladen Kis,[a] Yevhen Kozymka,[d] Sergey Linev,[a] Jan Orliński,[h] Giovanni Paternoster,[b] Christian Joachim Schmidt,[a] Luca Schramm,[a] Michael Traxler,[a] Michael Träger,[a] Szymon Treliński,[g] Yuanji Tian,[i] Felix Ulrich-Pur,[c,f] Matteo Centis Vignali[b] and Robert Visinka[a]

[a] *GSI Helmholtzzentrum für Schwerionenforschung GmbH, Darmstadt, Germany*
[b] *Fondazione Bruno Kessler, Trento, Italy*
[c] *Austrian Academy of Sciences, Marietta-Blau-Institut for Particle Physics, Vienna, Austria*
[d] *Technische Universität Darmstadt, Darmstadt, Germany*
[e] *Helmholtz Forschungsakademie Hessen für FAIR, Darmstadt, Germany*
[f] *TU Wien, Atominstitut, Vienna, Austria*
[g] *Institute of Nuclear Physics, Polish Academy of Sciences, Cracow, Poland*
[h] *Faculty of Physics at the University of Warsaw, Warsaw, Poland*
[i] *Hahn-Schickard-Gesellschaft für angewandte Forschung e.V., Villingen-Schwenningen, Germany*

E-mail: j.pietraszko@gsi.de

Abstract: This work presents the development and experimental validation of a novel thin (active layer thickness of 85 µm) double-sided strip Low-Gain Avalanche Detector (LGAD) prototype. We demonstrate a post-fabrication segmentation process where a standard single-sided LGAD sensor is micromachined to enable dual-sided signal extraction. Characterization using a dedicated front-end electronics system confirms strong spatial and temporal correlations between the junction and ohmic sides. The results validate that this architecture preserves the excellent timing performance of LGADs while providing a scalable solution for high-precision tracking in material-sensitive applications. By applying this procedure in conjunction with additional sensor thinning, a total sensor thickness below 50 µm can be achieved. To our knowledge, this represents the first implementation of a thin double-sided LGAD.

Keywords: Particle tracking detectors (Solid-state detectors); Timing detectors; Beam-line instrumentation (beam position and profile monitors, beam-intensity monitors, bunch length monitors); Instrumentation for particle-beam therapy

*Corresponding author.

https://doi.org/10.1088/1748-0221/21/07/C07022

2026 JINST 21 C07022

Contents

1 Introduction

Low-Gain Avalanche Detectors (LGADs) [1, 2] are widely used in modern experiments [3, 4] and continue to be improved in terms of radiation hardness, timing resolution, and detection efficiency. In many applications, however, the material budget is equally critical — for example in low-momentum particle tracking, medical imaging (e.g. ionCT) [5, 6], or fixed-target experiments for reaction time determination [4, 7] where detectors are placed directly in the primary beam. A promising approach to address these constraints is a double-sided strip configuration, well established in standard silicon detectors but not yet fully explored for LGADs. This geometry significantly reduces readout complexity: while pixel detectors require N^2 channels for a given area, double-sided strip sensors need only 2N, leading to substantially lower power consumption and frontend complexity while maintaining comparable performance. In this work, we present the principle of operation, a concept for realizing double-sided strip LGADs based on single-sided sensors, and the construction and characterization of a prototype. The approach is applicable to a wide range of sensor thicknesses and, to the best of our knowledge, represents the first implementation of thin double-sided LGADs.

2 Electrostatic principles of signal formation in double-sided sensors

To understand signal formation in the front-end electronics (FEE), we begin with an introduction to signal induction by a moving charge. This process can be understood intuitively using a classical electrostatic model of a point charge Q located at a distance h above an infinite conducting plane held at constant potential. As described for example in [8] the induced surface charge density on the plane is given by

$$\sigma(x, y, h) = -\frac{Qh}{2\pi(x^2 + y^2 + h^2)^{3/2}} \tag{2.1}$$

where: $\sigma(x, y, h)$ is the induced surface charge density on the electrode, Q is the magnitude of the point charge, h is the distance (height) of the charge above the conducting plane, x and y are the lateral coordinates on the surface of the electrode relative to the position of the charge. As shown in figure 1-Left this distribution is strongly localized around the point directly beneath the charge, in

2026 JINST 21 C07022

this example, for $h = 100\mu m$, most of the induced charge is confined within approximately $\pm 200\ \mu m$ in both transverse directions. The signal measured by the FEE is not the static charge itself, but rather the induced current. This current corresponds to the rate of change of the induced charge ($I = dQ/dt$) as the carrier traverses the detector volume. As the charge moves, it triggers a continuous rearrangement of the surface charge density; this dynamic process generates the current which, once amplified, is recorded by the FEE as a detectable signal.

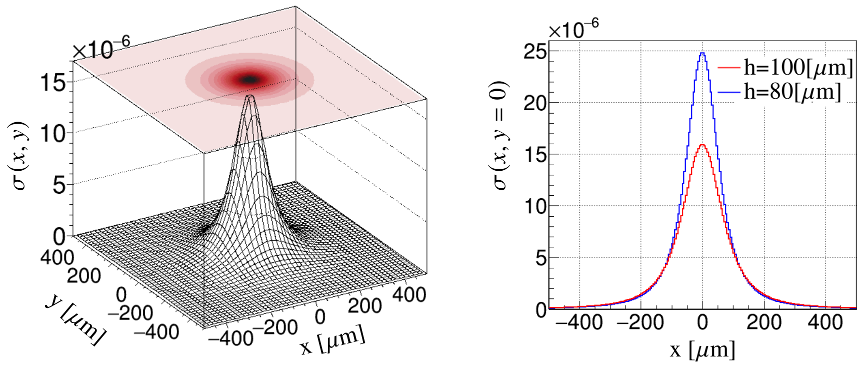

Figure 1. Left: Charge density distribution $\sigma(x, y)$ described by eq. (2.1) for $h = 100\ \mu m$ and $Q = -1$. Right: Transverse profile of the charge density along the x-axis (y=0) for $h = 100\mu m$ and $h = 80\mu m$. The comparison illustrates that the main charge redistribution occurs within $\pm 100\ \mu m$.

Using this simplified model of a point charge near a conductive plane, one can estimate the magnitude of the charge density rearrangement resulting from a displacement of 20 µm. To demonstrate this, we compare the projection of the charge distribution onto the x-axis for two different heights: $h = 100\ \mu m$ and $h = 80\ \mu m$. These distances are comparable to the typical drift displacement of charge carriers in LGAD sensors. As shown in figure 1-Right, the most significant changes in charge density occur within a narrow window of $\pm 100\ \mu m$. This suggests that the hit position can be precisely resolved, provided that the electrode segmentation is finer than 100 µm. In double-sided detectors, and in particular in double-sided LGADs, the sensor volume is enclosed between two conductive, segmented electrodes. Charge carriers — generated by ionizing radiation and subsequently multiplied in the gain layer — drift toward one electrode while simultaneously moving away from the other. Due to this geometry, the induced charge on the collecting electrode increases with one polarity, while the induced charge on the opposite electrode evolves with the opposite polarity. Consequently, the motion of a single charge carrier produces simultaneous bipolar signals on both electrodes.

The current generation in ionization detectors can be formally described by the Ramo-Shockley theorem [9, 10], which relates the induced current to the instantaneous motion of charge carriers and the electrode-specific weighting fields [2]. In double-sided architectures, the opposite signal polarities arise naturally from the complementary weighting fields of the two electrodes. Nevertheless, the simplified model presented in this section provides a highly intuitive description of the fundamental signal formation process in this type of sensor.

3 Segmentation and prototyping

To produce the double-sided LGAD demonstrator, we utilized single-sided strip sensors originally manufactured by Fondazione Bruno Kessler (FBK) for the HADES experiment [11]. The fixed-target

2026 JINST 21 C07022

HADES experiment utilizes a variety of beams, including pions, protons, and heavy ions, and employs multiple detector technologies for beam monitoring and reaction-time determination, such as diamond detectors [12–14] and LGAD sensors [4, 7]. The LGAD sensors used in this project had an active area of 8.6 mm × 8.6 mm and featured strip segmentation on the gain side with a 100 µm pitch. With a no-gain distance of approximately 24 µm, this design results in a fill factor of 74% on the primary readout side. The sensors were thinned at the wafer level to a total thickness of 200 µm, with an active layer thickness of 85 µm. In a typical $n^{++}/p^{+}/p/p^{++}$ thin LGAD architecture — as described for example by Cartiglia et al. [2] — the active sensor volume is supported by a relatively thick, low-resistivity p^{++} substrate. This substrate is usually coated with an Aluminum (Al) or Gold (Au) layer to facilitate electrical contact and wire bonding.

To achieve true double-sided functionality, both the top (junction side) and the bottom (ohmic side) electrodes must be segmented. While the junction side was pre-segmented with a 100 µm pitch at FBK our research focused on the back-side segmentation of the p^{++} support layer. A critical electrical requirement for this process is that the individual segments must maintain an inter-electrode isolation resistance of at least several kΩ. To satisfy this requirement, the segmentation must not only penetrate the metallization but must also extend entirely through the low-resistivity p^{++} substrate to ensure effective electrical isolation between individual segments. In our approach, we performed this deep segmentation of the p^{++} layer to ensure high electrical isolation. The precision machining for this segmentation was carried out at the Hahn-Schickard-Gesellschaft für angewandte Forschung e.V. in Villingen-Schwenningen, Germany and is shown in figure 2-(Right). A side view of the segmented back-side is shown in figure 3. Direct inspection via optical microscopy was used to characterize the dimensions of the machined structures. The measured total thickness of the sensor in this sample was found to be 189.6 µm, slightly lower than the nominal wafer thickness of 200 µm specified by the manufacturer. This difference is attributed to the inherent tolerances in the thinning process and the limited precision of the microscopic measurement, which was performed with the sensor tilted to capture the trench topography. The primary objective of the back-side processing was to ensure robust electrical isolation between adjacent segments. As visible in the figure, the isolation trenches were

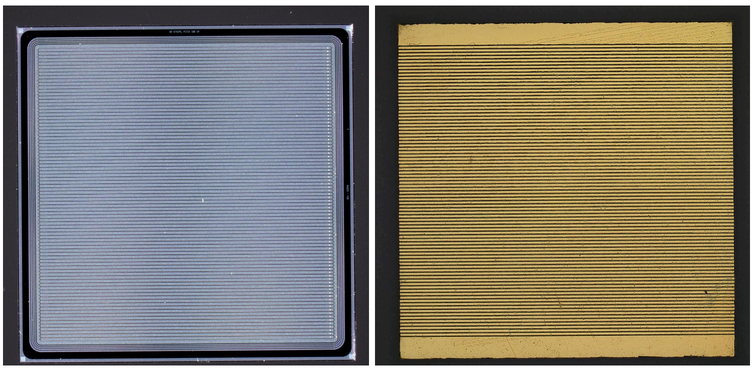

Figure 2. Surface Segmentation of the Double-Sided LGAD Prototype. Left: The original junction-side strip segmentation (100 µm pitch) as originally manufactured at FBK for the HADES experiment. Right: The custom backside segmentation machined at the Hahn-Schickard-Gesellschaft. The parallel strips were produced with a matching 100 µm pitch, aligned parallel to the junction-side strips, ensuring deep isolation through the p^{++} support layer.

2026 JINST 21 C07022

machined to a depth of 117.4 μm. Given that the p^{++} support layer was thinned to a nominal depth of approximately 115 μm, these trenches successfully penetrate the low-resistivity substrate to reach the active layer. This deep-trench architecture is critical; by fully traversing the p^{++} layer, we eliminate the low-resistance lateral paths, thereby ensuring that each readout segment is electrically isolated. Four single-sided LGAD sensors were successfully mechanically processed. The produced trenches were not terminated in any way and remained air-isolated during the entire characterization phase. Open defects present in the trenches are a source of increased dark current, which for these sensors reached 100 − 150 μA. In addition, variations of up to 20% over time were observed, indicating a possible influence of humidity on the device performance.

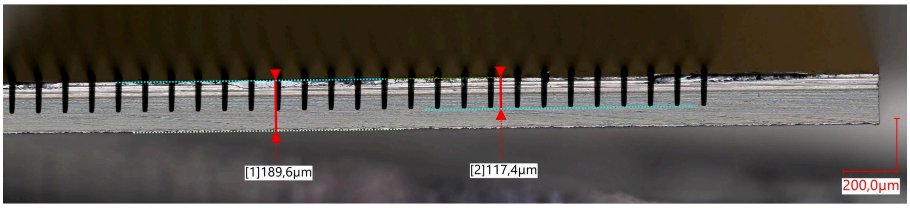

Figure 3. Cross-sectional view of the back-side segmentation. The measured sensor thickness of 189 μm (nominally 200 μm) and trench depth of 117 μm are indicated. The discrepancy in total thickness is attributed to microscopic measurement perspective and thinning tolerances. The 117 μm trenches are designed to fully traverse the p^{++} support layer and reach the active volume, ensuring effective electrical isolation between segments.

4 Front-end electronics and High-Voltage biasing

To evaluate the performance of the double-sided LGAD prototype, a dedicated FEE system was developed. The FEE must satisfy three primary functional requirements: high-gain signal amplification, stable High-Voltage (HV) biasing, and reliable decoupling of the fast signals from the high-potential side. The baseline FEE architecture for single-sided LGAD sensors is described in detail in [14]. For this study, we implemented specific modifications to accommodate the requirements of a double-sided readout. Specifically, to enable segmentation on the back-side (ohmic side), the FEE must provide a common HV bias to every strip while simultaneously maintaining individual signal paths for each segment. A critical constraint in this design is the maintenance of inter-strip electrical isolation, which must remain in the several kΩ range to prevent signal crosstalk. The concept of double-sided signal extraction is well-established in detector literature [15], with prominent large-scale implementations such as the CBM silicon strip tracker [16]. In the CBM design, AC coupling is integrated directly into the sensor using a dielectric stack (typically SiO_2 and Si_3N_4) with aluminum strips, while HV biasing is provided via integrated polysilicon bias resistors distributed across the strips. In contrast, for our prototyping phase, these functionalities were moved from the sensor level to the PCB level. We utilized discrete HV-rated coupling capacitors for AC decoupling and high-value resistors for HV distribution, mounted directly on the interface PCB upstream of the amplifiers. This discrete approach allowed for maximum flexibility in testing the isolation and signal-sharing characteristics of the micromachined strips. The micromachined double-sided strip LGAD was interfaced to the readout PCB via aluminum wire bonding, as shown in figure 4. In the current PCB configuration, 64 channels were instrumented on each side of the sensor. Given the 100μm strip pitch and the

2026 JINST 21 C07022

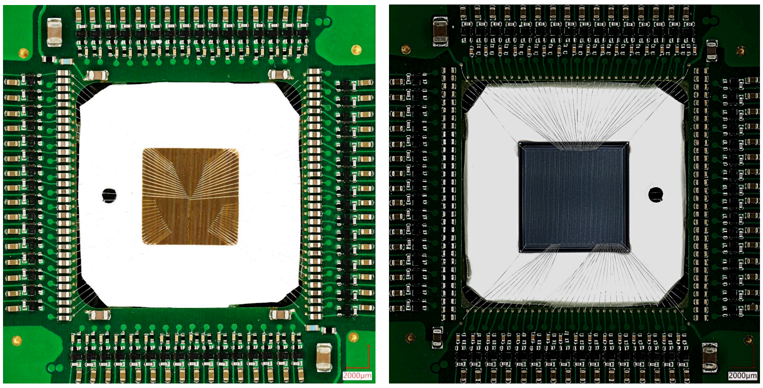

Figure 4. Top and bottom views of the double-sided LGAD prototype mounted on a dedicated readout PCB. The assembly incorporates integrated AC coupling, bias resistors, and two-stage amplification for both signal paths.

total active area, this corresponds to a subset of the 86 available strips on the junction side. To preserve electric-field uniformity and ensure stable sensor operation, the non-instrumented strips were connected to a common ground (GND) rather than left floating.

5 Performance characterization of the double-sided LGAD prototype with a ^{90}Sr source

In an initial step, the analog signals — after two stages of amplification — were observed using an oscilloscope. The setup was optimized to highlight features characteristic of double-sided sensors. For this study, four channels were selected: one channel on the junction (Al) side and three channels on the ohmic (HV) side, located directly beneath the selected Al-side channel. This configuration was possible because the segmentation on the HV side was aligned parallel to the strip orientation on the Al side. Figure 5 shows the waveforms from all four channels, triggered by a negative-polarity signal on channel 1, with the sensor irradiated by a ^{90}Sr radioactive source. As expected, the corresponding channel on the HV side (channel 2) exhibits a time-correlated signal with opposite (positive) polarity. In contrast, the two neighboring strips show no significant signals, consistent with the highly localized nature of signal formation in this type of sensor. The signal amplitudes on the corresponding channels are also correlated, as illustrated in figure 5 for both high- and low-amplitude events. In the next step, the detector was connected to the Data Acquisition (DAQ) system. Each strip is read out through three amplification stages, followed by a leading-edge discriminator connected to a TDC. The discriminator and TDC are implemented in an FPGA; further details can be found in [6]. For this type of readout, additional data analysis is essential, including time-offset and time-walk corrections, which were performed following the procedure described also in [6]. With strips from both sides connected to the DAQ system, the Al side was used as the trigger while the sensor was irradiated with a ^{90}Sr source. In this procedure, for each cluster identified on the Al side, all clusters on the Au side were examined, and the correlation plot shown in figure 6-Left was constructed. The plot shows the strip position (number) for cluster pairs on both sides and demonstrates the expected one-to-one correlation, consistent with the principle of operation. It can also be observed that, in three regions, the correlation width is approximately two channels, in contrast to the single-channel correlation seen elsewhere. This behavior indicates incomplete electrical isolation of the strips on the HV side, with some strips

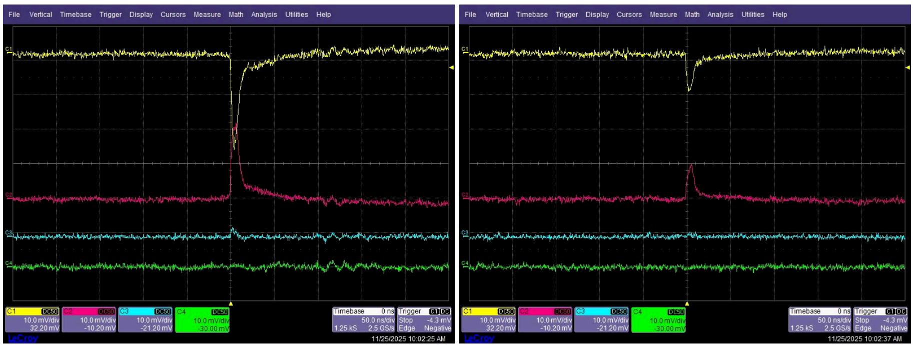

Figure 5. Scope traces from four channels for two events (high and low amplitude), demonstrating time-correlated bipolar signals on opposite electrodes.

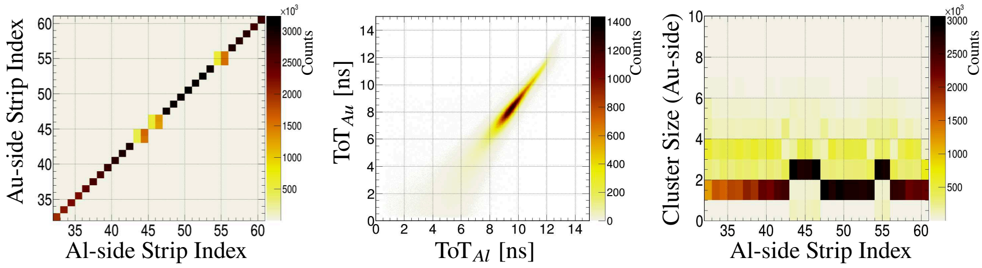

Figure 6. Dual-sided signal correlations for coincidence events. Left: Spatial correlation between the hit channel indices on the junction (Al) and ohmic (Au) sides. Middle: Correlation of the Time-over-Threshold (ToT) values from both sides. Right: Cluster size on the Au-side as a function of the Al-side hit channel.

effectively shorted through a low-resistance path. This finding highlights the need for high-precision segmentation and further optimization of the processing.

Using the correlated strip pairs, we investigated the signal amplitude dependence between the Al and Au sides. The readout electronics do not measure the signal amplitude directly; instead, the discriminator output width provides Time-over-Threshold (ToT) information, which serves as an indirect measure of the signal amplitude. Figure 6-Middle shows the ToT correlation for strip pairs (selected strip 50 on each side) on opposite sides of the sensor. The strong correlation observed confirms that the signals on both sides originate from the motion of the same charge carriers generated in the sensor by an ionizing particle. In a similar manner, we investigated the cluster size of signals recorded on the HV side. The results are shown in figure 6-Right. The distribution is dominated by single-strip clusters, as expected. In addition, three groups exhibit cluster sizes of two, confirming that some neighboring strips are electrically connected due to imperfect segmentation. Larger cluster sizes can be attributed to capacitive coupling, a characteristic feature of strip detectors with closely spaced electrodes. Using the same data sample, we investigated the timing performance of the sensor. For this purpose, a pair of geometrically corresponding strips — one on the top (Al) side and one on the bottom (Au) side — aligned parallel and directly overlapping — was selected, and the time difference between the recorded signals was plotted as a function of ToT (figure 7-Left). The horizontal trend of the distribution indicates that the time-walk correction has been properly applied. By projecting the distribution onto the y-axis, the time resolution was extracted, as shown in figure 7-Right. The

2026 JINST 21 C07022

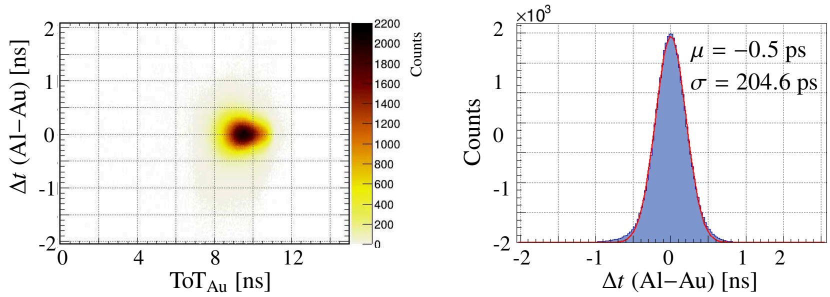

Figure 7. Left: Correlation between the time difference Δt (strip 41, Al vs. Au) and the signal Time-over-Threshold (ToT) from the Au-side. Right: Y-axis projection of the distribution, fitted with a Gaussian function. The fit yields a mean offset $\mu \approx 0$ and a temporal resolution $\sigma \approx 205$ ps.

obtained value of 204.6 ps is higher than the expected performance and can be attributed to several factors: (1) the bonding scheme, in which the readout strips on the two sides are not connected at the same longitudinal position, introducing an additional time contribution from signal propagation; (2) an increased electronic jitter; (3) distortions of the electric field caused by field-free regions between parallel strips on both sides; and (4) elevated sensor noise due to a high dark current. Further detailed studies are planned to systematically investigate these sensor properties.

6 Summary

In this contribution, we have presented the concept, fabrication, and performance of a prototype double-sided LGAD sensor. Measurements using a ^{90}Sr source show excellent agreement with the expected performance, confirming the validity of the design. Further improvements are foreseen, in particular through optimized trench fabrication techniques aimed at reducing dark current. Future studies will focus on detailed timing characterization using external tracking systems and proton beam tests. In parallel, we plan to develop new double-sided strip sensors based on trench-isolated single-sided LGADs, targeting an effective fill factor close to 100%. Additional thinning of the sensors to a total thickness of approximately 50 µm is also foreseen. This will constitute a significant step towards ultra-thin, high-precision, low-mass 4D tracking detectors.

Acknowledgments

This research was funded in part by the Austrian Science Fund (FWF) Erwin-Schrödinger Grant Nr. J 4762-N, GSI-TU Darmstadt F&E, DFG IGRK 2891, Polish NSC-grant OPUS no. 2023/49/B/ST2/00652 and the European Union's Horizon 2020 research and innovation programme under grant agreement no 824093 (STRONG2020) and 871072. The financial support of the Austrian Ministry of Education, Science, and Research is gratefully acknowledged for providing beam time and research infrastructure at MedAustron. The publication is funded by the Open Access Publishing Fund of GSI Helmholtzzentrum fuer Schwerionenforschung.

2026 JINST 21 C07022

References

[1] G. Pellegrini et al., *Technology developments and first measurements of Low Gain Avalanche Detectors (LGAD) for high energy physics applications*, Nucl. Instrum. Meth. A **765** (2014) 12.

[2] N. Cartiglia et al., *Design optimization of ultra-fast silicon detectors*, Nucl. Instrum. Meth. A **796** (2015) 141.

[3] N. Moffat et al., *Low Gain Avalanche Detectors (LGAD) for particle physics and synchrotron applications*, 2018 *JINST* **13** C03014.

[4] J. Pietraszko et al., *Low Gain Avalanche Detectors for the HADES reaction time (T_0) detector upgrade*, *Eur. Phys. J. A* **56** (2020) 183 [arXiv:2005.12965].

[5] F. Ulrich-Pur et al., *Novel ion imaging concept based on time-of-flight measurements with low gain avalanche detectors*, 2023 *JINST* **18** C02062 [arXiv:2209.13676].

[6] F. Ulrich-Pur et al., *First experimental time-of-flight-based proton radiography using low gain avalanche diodes*, *Phys. Med. Biol.* **69** (2024) 075031 [arXiv:2312.15027].

[7] W. Krüger et al., *LGAD technology for HADES, accelerator and medical applications*, Nucl. Instrum. Meth. A **1039** (2022) 167046.

[8] D.J. Griffiths, *Introduction to Electrodynamics*, 3rd edition, Upper Saddle River, NJ, Prentice-Hall, Inc. (1999).

[9] S. Ramo, *Currents induced by electron motion*, *Proc. Ire.* **27** (1939) 584.

[10] W. Shockley, *Currents to Conductors Induced by a Moving Point Charge*, *J. Appl. Phys.* **9** (1938) 635.

[11] HADES collaboration, *The High-Acceptance Dielectron Spectrometer HADES*, *Eur. Phys. J. A* **41** (2009) 243 [arXiv:0902.3478].

[12] J. Pietraszko et al., *Diamonds as timing detectors for MIP: The HADES proton-beam monitor and start detectors*, Nucl. Instrum. Meth. A **618** (2010) 121 [arXiv:0911.0337].

[13] J. Pietraszko et al., *Radiation damage in single crystal CVD diamond material investigated with a high current relativistic ^{197}Au beam*, Nucl. Instrum. Meth. A **763** (2014) 1.

[14] J. Pietraszko et al., *LGAD technology for heavy ion detection and radiation damage diagnostics in diamond*, 2025 *JINST* **20** C08007.

[15] H. Spieler, *Semiconductor Detector Systems*, Oxford University Press (2005) [DOI:10.1093/acprof:oso/9780198527848.001.0001].

[16] A. Rodríguez Rodríguez et al., *Functional characterization of modules for the Silicon Tracking System of the CBM experiment*, Nucl. Instrum. Meth. A **1058** (2024) 168813.

2026 JINST 21 C07022